Electronic Supplementary Material (ESI) for Nanoscale.

Supplementary Information

Multidimensional characterization of noble metal alloy nanoparticles by multiwavelength analytical ultracentrifugation

P. Cardenas Lopez,[a,b] M. J. Uttinger,[a,b] N. E. Traoré,[a,b] H. A. Khan,[c] D. Drobek,[d] B. Apeleo Zubiri, [d] E. Spiecker, [d] L. Pflug,[c] W. Peukert [a,b] and J. Walter*[a,b]

a) *Institute of Particle Technology (LFG), Friedrich-Alexander-Universität Erlangen-Nürnberg (FAU), Cauerstr. 4, 91058 Erlangen, Germany.*
b) *Interdisciplinary Center for Functional Particle Systems (FPS), Friedrich-Alexander-Universität Erlangen-Nürnberg (FAU), Haberstr. 9a, 91058 Erlangen, Germany.*
c) *Competence Unit for Scientific Computing (CSC), Friedrich-Alexander-Universität Erlangen-Nürnberg (FAU), Martensstr. 5a, 91058 Erlangen, Germany.*
d) *Institute of Micro- and Nanostructure Research (IMN) & Center for Nanoanalysis and Electron Microscopy (CENEM), Interdisciplinary Center for Nanostructured Films (IZNF), Friedrich-Alexander-Universität Erlangen-Nürnberg (FAU), Cauerstr. 3, 91058 Erlangen, Germany.*

*Corresponding author: johannes.walter@fau.de

Optical modelling: Empirical constant C

Compilation of empirical constant *C* values available in the literature. Here we show exclusively those declared for spheres.

Table S1. C values reported in the literature for spheres and values retrieved for this study. Modified from Kreibig et al.[1]

Theory	Method	C value for spheres	Researchers
Maxwell theory: Drude dielectric function with free path limitation	Isotropic scattering	1	Kreibig[2]
	Isotropic scattering	0.3701 (for Ag)	This work
	Isotropic scattering	0.4059 (for Au)	This work
	Diffuse scattering	0.75	Kreibig[2]
Discrete energy levels	Fluctuation-Dissipation theorem	0.29 (for Ag)	Kawabata et al.[3]
Quantum box model		1	Genzel et al.[4]
		0.5	Ruppin and Yatom[5]
		0.93	Wood and Ashcroft[6]
		1.16	Kraus and Schatz[7]
Electrodynamic theory	Electron density, smooth profile	1	Appel and Penn[8]

Complex refractive indices of Ag, 50 % GMF Ag-Au alloy, and Au

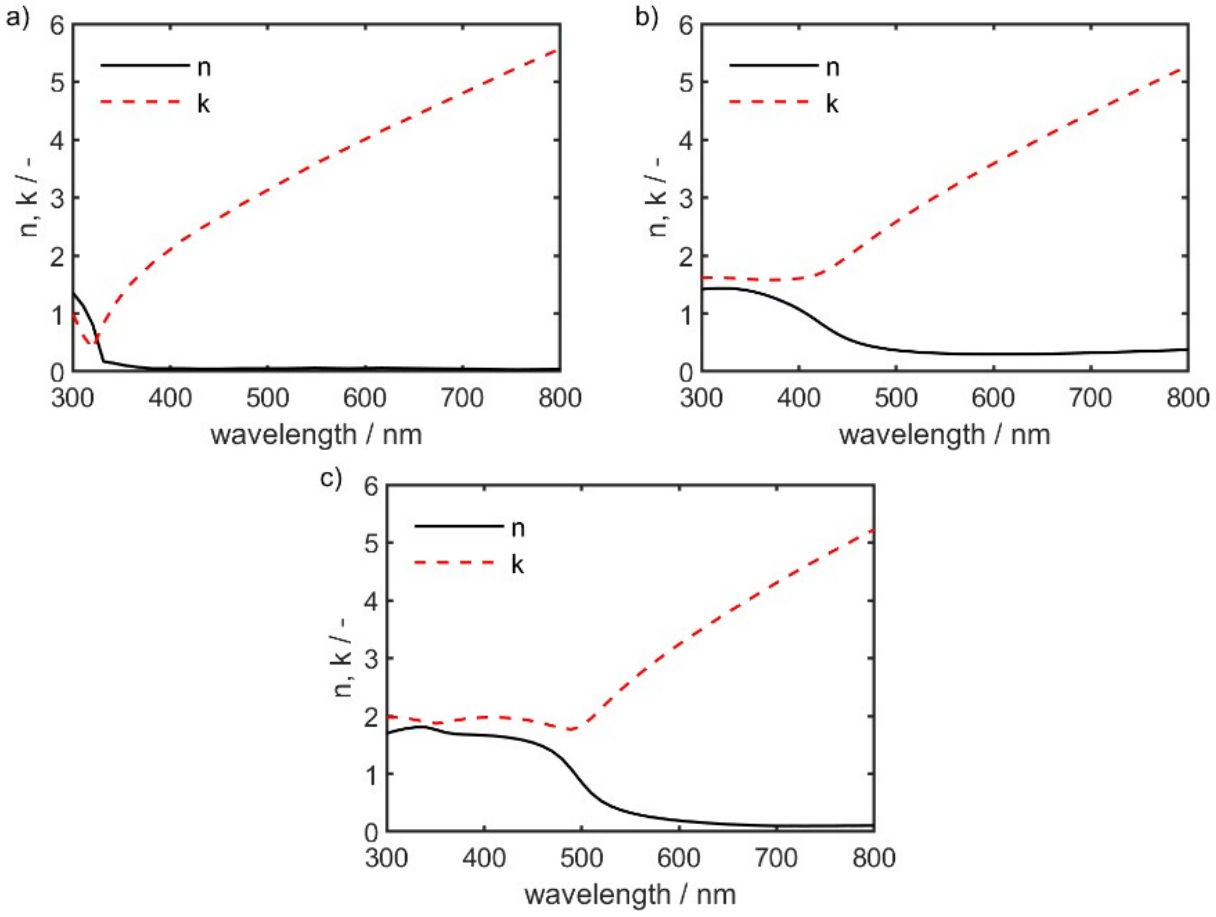

Figure S1. Bulk refractive indices real part (n) and imaginary part (k) values for a) Ag[9] b) 50 % Au molar fraction (GMF) alloy[10], and c) Au[11].

Determination of shell thickness from sedimentation velocity (SV) analytical ultracentrifugation (AUC) experiments and scanning transmission electron microscopy (STEM) analysis

In a first step, we approached the citrate shell thickness by conducting SV-AUC experiments followed by combined sedimentation-diffusion analysis according to the work of Carney et al.[12] in SEDFIT, see Figure S2. However, due to the high density of the nanoparticles (NPs) and their comparably large size, resulting in little diffusion information, an accurate fit for the partial specific volume via SEDFIT could not be achieved. Consequently, the shell thickness of the NPs could not be determined via this method. This observation is further assessed with the retrieval of the dimensionless Peclet (Pe) number, defined as the ratio of sedimentation and diffusion fluxes of the NPs. Generally speaking, it is possible to asses both sedimentation and diffusion properties at intermediate Pe numbers. At small Pe numbers, however, the NPs in motion are mostly driven by diffusion, disabling the assessment of sedimentation properties. On the contrary, at large Pe numbers, the motion of the NPs is dominated by sedimentation, making impossible to extract diffusion properties from the sedimentation data. Uttinger et al.[13] stated that during analytical centrifugation measurements of Au NPs of the same magnitude as the ones employed in our study, a successful sedimentation and diffusion analysis can be made from sedimentation boundaries for Pe>1 and Pe<100.[13] In our case, the large Pe numbers of 80.32 for the Ag measurement and 155.87 for the Au measurement further confirm this observation.

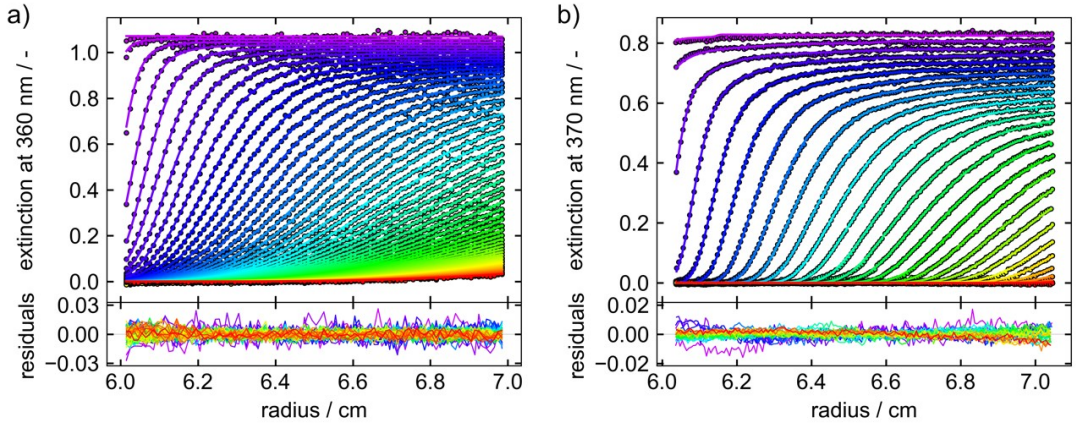

Figure S2. Representative sedimentation velocity data and residuals of the validation experiments for a) 20 nm Ag NPs (λ = 360 nm) and b) 20 nm Au NPs (λ = 370 nm).

In a second step, we compared the particle core size distributions obtained from SV-AUC and STEM. To yield the solvated citrate shell thickness for each particle sample, we developed a fitting algorithm, which seeks for the smallest difference between the modal particle core diameters by AUC and STEM. This led to $h_{shell,\ Ag}$ = 1.94 nm and $h_{shell,\ Au}$ = 2.19 nm, when considering a shell which is composed of 50 wt. % citrate and 50 wt. % water. The respective core diameter distributions are depicted in Figure S3. For sake of simplicity and given that the difference between both shell thicknesses is merely 2.5 Å, we proceed with our calculations further on with an average citrate shell thickness of $h_{shell,\ NP}$ = 2.0 nm.

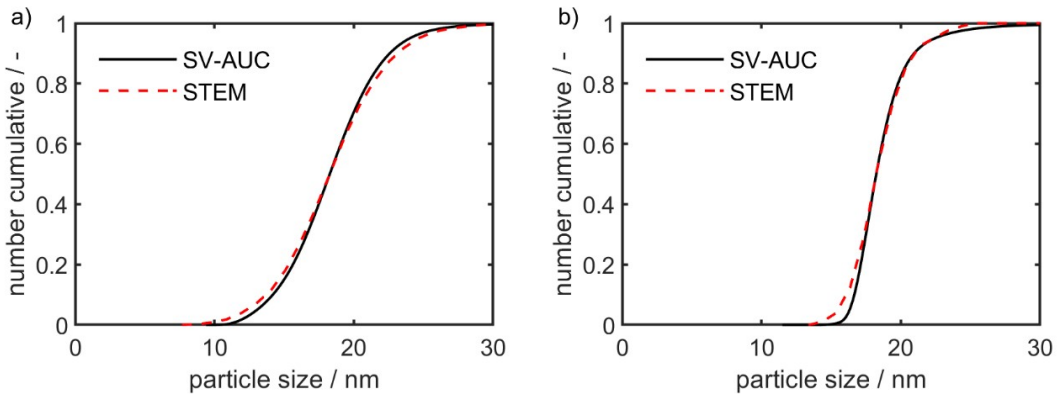

Figure S3. Number cumulative distributions from SV-AUC and STEM for a) 20 nm Ag NPs and b) 20 nm Au NPs. The best fit h_{shell} values of 2.0 nm and 2.2 nm for Ag and Au NPs, respectively, were derived via minimization of the median particle core sizes using STEM as benchmark.

Influence of shell refractive index on ensemble optical spectra

To investigate the effect of the shell layer's optical properties on the ensemble spectra, we have performed forward Mie core-shell calculations. Here we simulated a shell thickness of 2 nm above the noble metal NP, with a citrate refractive index of 1.509[14] (at T = 20 °C) and the wavelength-dependent Sellmeier coefficients of water at T = 20 °C from Daimon and Masumura[15].

In analogy to the work shown in the main manuscript, we approximate simulated spectra to spectra obtained by UV-Vis spectroscopy with a fitting algorithm. In this case, we yield C_{Ag} = 0.3490 and C_{Au} = 0.3424. Obtained spectra are shown in Figure S4.

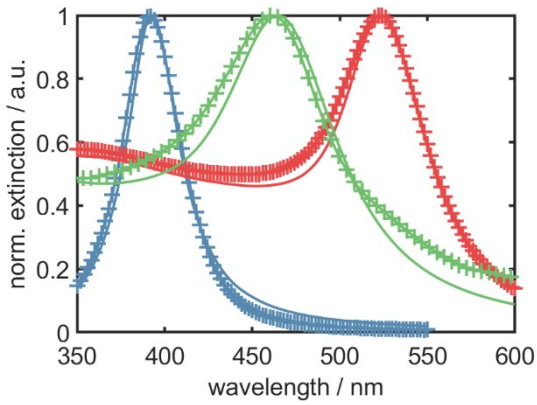

Figure S4. Experimentally measured spectra (cross-marked lines) and calculated spectra (solid lines) with basis on Mie's core-shell model for 20 nm Ag NPs (blue), 40 nm 50 % GMF alloy NPs (green), and 40 nm Au NPs (red).

Although the core-shell model approximates the experimental spectra partly well, deviations appear in some regimes of the spectrum. These deviations can also arise due to the non-considered wavelength-dependent refractive indices of citrate, which to the best of our knowledge are not available in the literature. Furthermore, specific absorption of the bound ligand molecules and limitations for the application of a continuum model for modelling of a soft shell can also play an important role.

In order to proceed with the best suited optical modelling, we calculated the root-mean-square deviation (RMSD) between Mie core- and Mie core-shell-simulated and experimental spectra for Ag and Au. The results are shown in Table S2 and indicate that the shell, while being of large importance for the hydrodynamic properties of the NPs, appears insignificant for the optical response of the particles. The RMSD is found to be even smaller for the Mie core simulations, so we proceeded with the simpler model to predict the optical spectra for the optical back-coupling (OBC) analysis.

Table S2. C and RMSD values for Ag and Au in Mie core and Mie core-shell spectra calculations.

	Mie core		Mie core-shell	
	C	**RMSD**	**C**	**RMSD**
Ag	0.3701	0.0256	0.3490	0.0273
Au	0.4059	0.0075	0.3424	0.0089

Influence of particle anisotropy on the optical spectrum investigated by discrete dipole approximation (DDA) simulations

In order to study the effect of shape anisotropies, the optical properties of oblate and prolate ellipsoidal particles with aspect ratios of 0.8 and 1.2, respectively, have been numerically approximated. The size of both particles was chosen so that they have the volume of an equivalent 30 nm diameter sphere. A numerical averaging over all oriental directions was performed by the Romberg quadrature scheme. The simulations of the extinction cross sections for the non-spherical NPs were performed by the Discrete Dipole Approximation Method using the ADDA package[16].

The refractive index of the surrounding material, i.e., water, was chosen to be n = 1.33, the refractive index of Au was given by Johnson and Christy[9]. The studied wavelength range from 300 nm to 1300 nm was discretized in 2.5 nm steps, the polarization used was derived from Clausius-Mossotti[16] and the particles were discretized in dipoles with 0.3 nm size, resulting in a total number of approximately 0.5 million dipoles.

As can be seen in Figure S5, the change of the NPs anisotropy leads to a slight shift of the peak maximum. Assuming a particle shape distribution in terms of the anisotropies would thus result in a peak broadening.

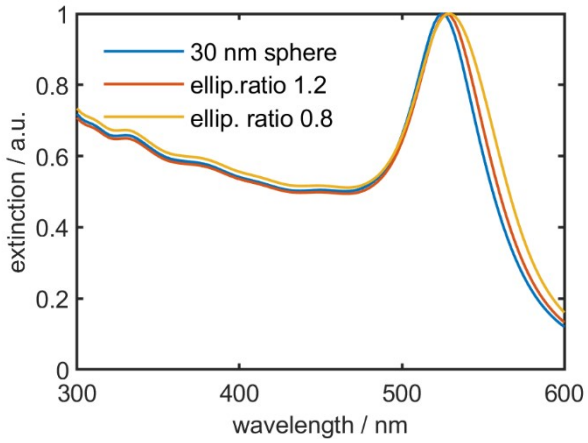

Figure S5. Influence of particle shape anisotropy on Au NPs spectra.

Influence of composition inhomogeneity on the optical spectrum investigated by DDA simulations

In order to probe composition inhomogeneity of Au and Ag in the NPs and the related effect on the optical spectra, a study of the extinction cross-sections of differently composed but radially symmetric alloy NPs was performed. The simulations are based on the transfer-matrix method implemented in the STRATIFY package[17].

The used refractive index of Ag-Au alloys was based on Rioux et al[10]. The particles were discretized in 100 uniformly distributed shells. In each shell the volume weighted mean Ag-Au composition was computed for the in Figure S6 shown GMF curves. Based on these mean values, the corresponding Ag-Au refractive index was computed.

The particles considered had a 50 % GMF and have a diameter of 30 nm. The composition ranges from an Au core and Ag shell over linear gradients up to an Ag core and an Au shell. The effect of the composition inhomogeneity on the extinction cross section is evident, see Figure S6. As evidenced by the simulated spectra, it can be inferred that a slight composition inhomogeneity along the radial dimension will lead to broadening of the spectrum, while the peak position remains constant. In consequence, the average composition can still be correctly retrieved from the spectrum. In contrast, completely different spectra are retrieved for the two extreme cases of a core-shell particle.

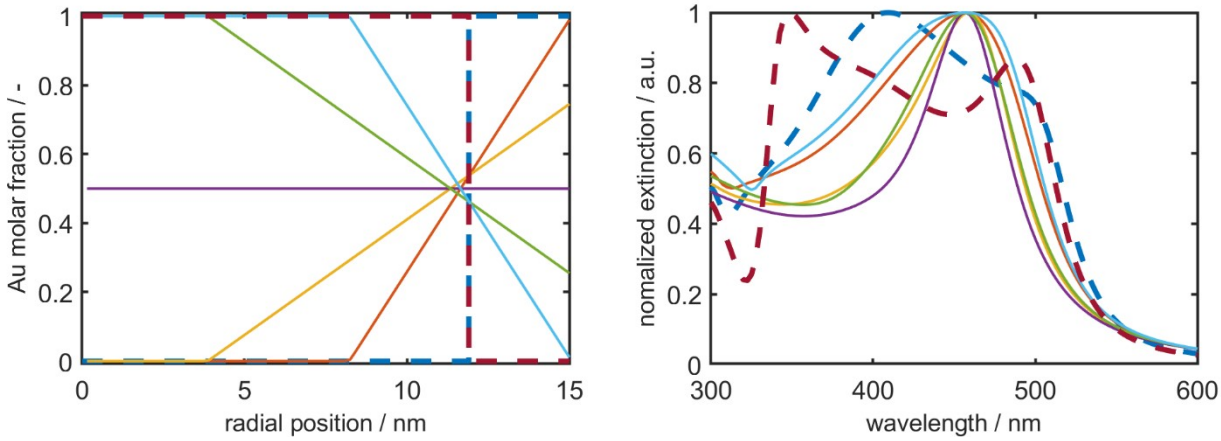

Figure S6. Left: GMF distribution for 30 nm diameter 50 % GMF alloy NP. Right: Computed normalized extinciton for Ag-Au alloy NPs with compositon inhomogeneity according the compositional distributions depicted in the left panel.

Chemical composition analysis of alloy particle using cross-section STEM-energy dispersive X-ray spectroscopy (STEM-EDXS)

STEM-EDXS measurements (2D mapping) have been performed to obtain a precise analysis of the local chemical composition of a selected Ag-Au alloy NP. For this purpose, as described in the main manuscript, a thin cross-section lamella through a selected Ag-Au alloy NP was prepared. A larger piece around the selected particle including the substrate was cut off from the wafer with the focused ion beam (FIB) and transferred using the so-called FIB lift-out technique to a lift-out TEM grid (PELCO Indicator). Finally, the particle was thinned down by FIB milling from both sides to a thickness of about 40 nm, allowing for a local and precise STEM-EDXS analysis.

Figure S7a shows the selected particle in cross-section in high-angle annular dark-field STEM. The corresponding STEM-EDXS map (Figure S7b) shows in general a good homogeneity and evenly mixed distribution of Ag and Au inside the particle, which can be seen in the corresponding line profiles from top to bottom in Figure S7c (blue dotted lines) and from left to right in Figure S7d (pink dotted lines). This confirms a general homogeneity with a small Au enrichment in the core and an Ag enrichment on the outer side of the NP, the latter being more pronounced on the upper part of the particle. The measured particle chemical composition of 48 % GMF also agrees well with the as targeted composition of 50 % GMF.

The favored Ag enrichment on the outer sides can possibly be explained by the lower surface energy of Ag (78 meV A^{-2}) in comparison to Au (97 meV A^{-2}). Combined with the higher cohesive energy of Au (3.81 eV/atom) versus Ag (2.95 eV/atom) and the weak exothermic enthalpies of the Ag-Au alloy NPs during formation, indicating the enrichment of Au in the core due to the preference of Au-Au metal bonds over Ag-Au and Ag-Ag.[18]

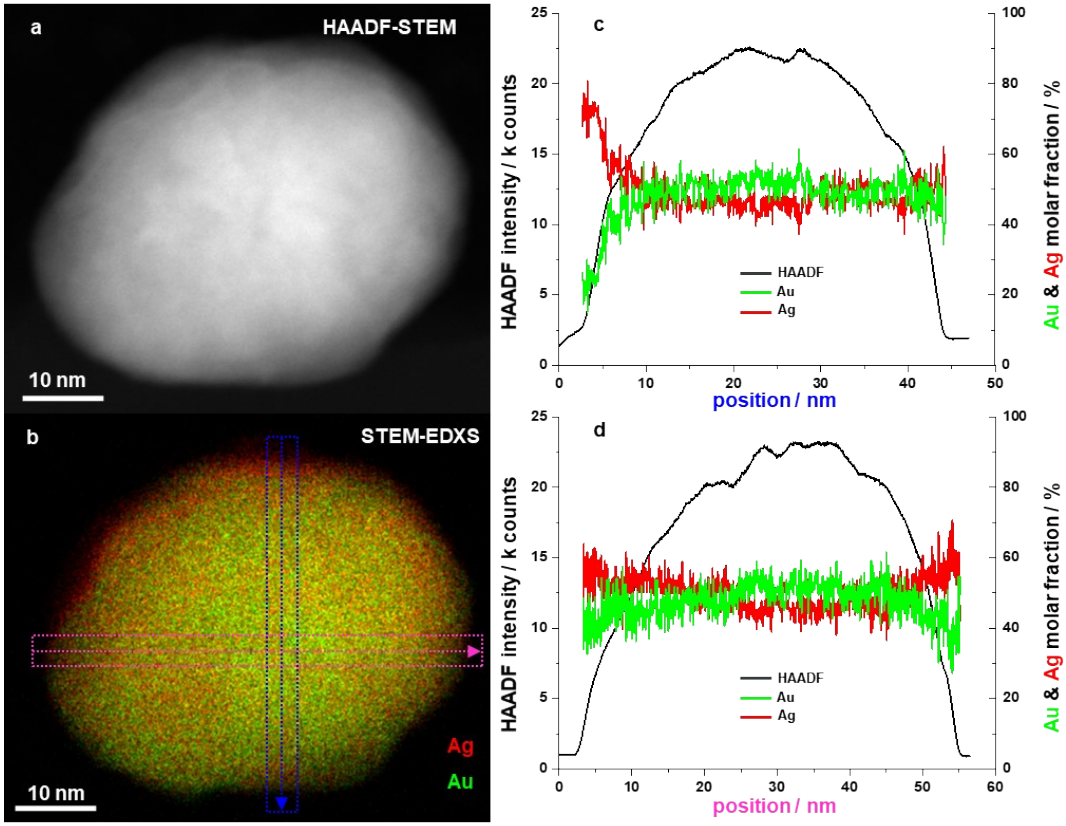

Figure S7. Chemical composition analysis of a 50 % GMF Ag-Au alloy NP in cross-section, using STEM-EDXS. a) HAADF-STEM image of the particle in cross-section. b) STEM-EDXS map of the particle with Au-signal labelled in green and Ag in red. c) The EDXS line profile through the particle cross section from top to bottom, as indicated with blue dotted lines in b) (HAADF signal black, Ag red and Au green lines), shows a homogeneous mixing behavior with a small enrichment of gold in the core and silver on the outer sides, which is more pronounced at the top of the particle. d) The EDXS line profile through the particle cross section from left to right, as indicated with pink dotted lines in b) (HAADF signal black, Ag red and Au green lines), shows a homogeneous mixing behavior with a small enrichment of gold in the core and silver on the outer sides.

2D distributions from synthetic AUC data

Ag NPs

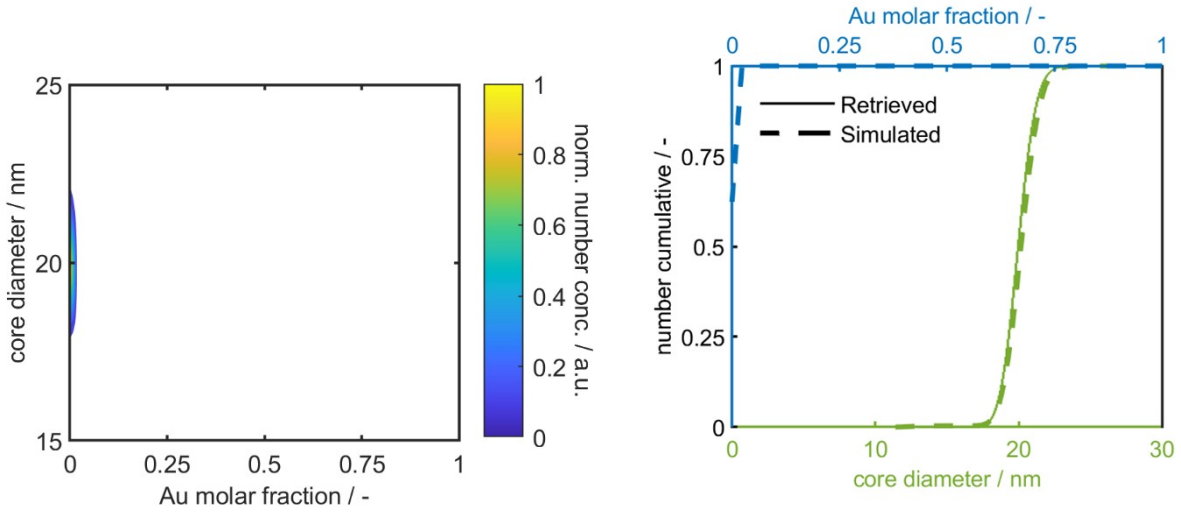

Figure S8. Left: 2D size-composition distributions for 20 nm Ag particles obtained by OBC analysis of synthetic data. Right: Respective marginalized number weighted cumulative distributions as function of diameter (green) and composition (blue).

Ag-Au alloy NPs

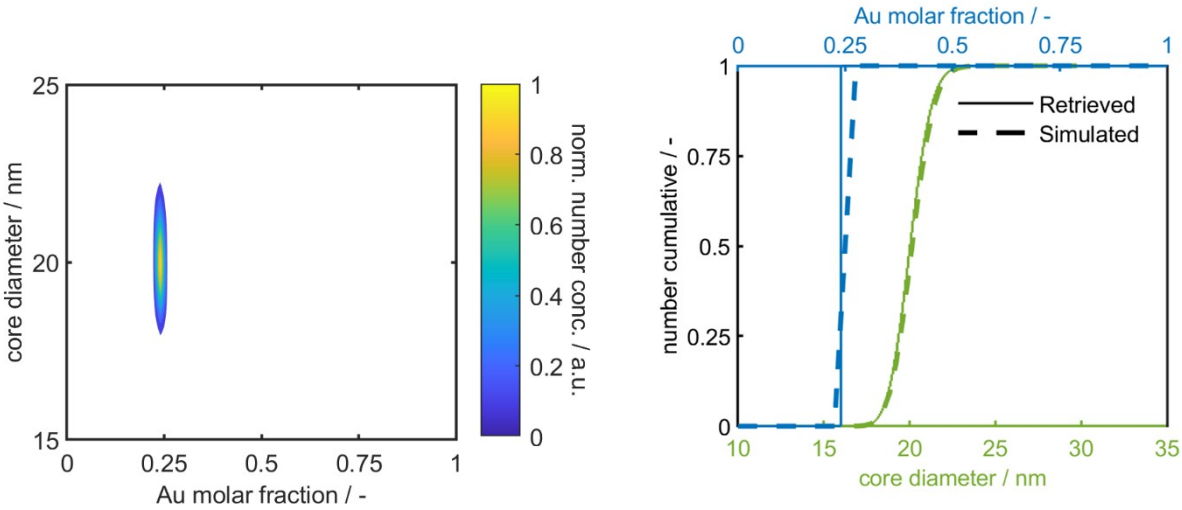

Figure S9. Left: 2D size-composition distributions for 20 nm 25 % GMF alloy NPs obtained by OBC analysis of synthetic data. Right: Respective marginalized number weighted cumulative distributions as function of diameter (green) and composition (blue).

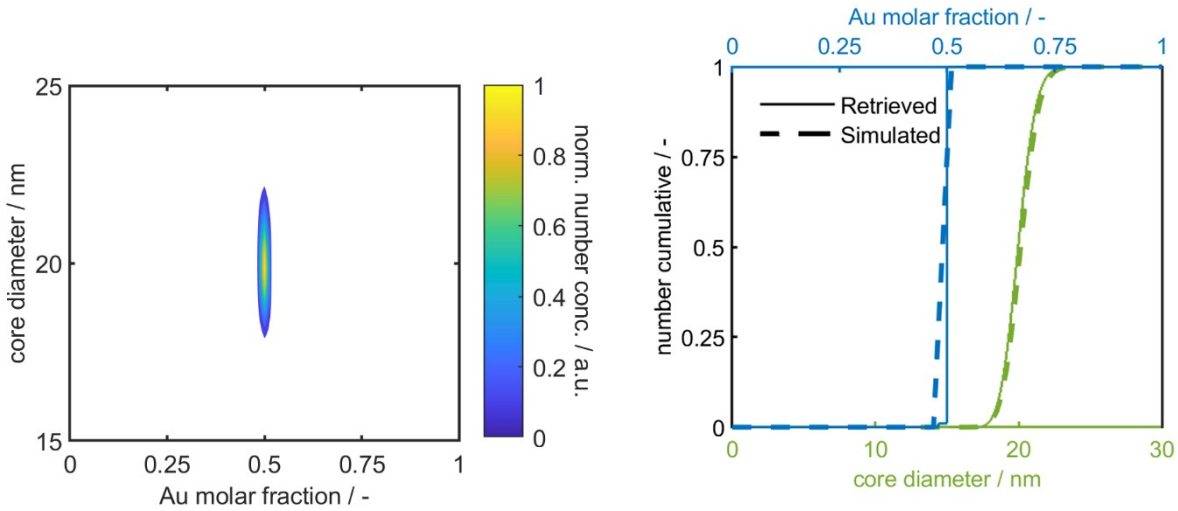

Figure S10. Left: 2D size-composition distributions for 20 nm 50 % GMF alloy NPs obtained by OBC analysis of synthetic data. Right: Respective marginalized number weighted cumulative distributions as function of diameter (green) and composition (blue).

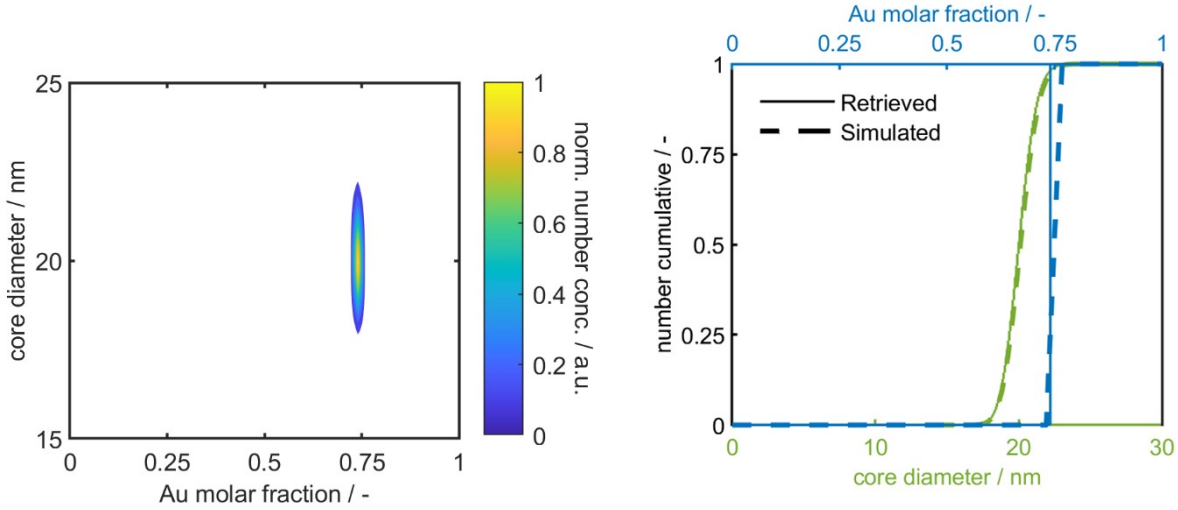

Figure S11. Left: 2D size-composition distributions for 20 nm 75 % GMF alloy NPs with 75 % Au content obtained by OBC analysis of synthetic data. Right: Respective marginalized number weighted cumulative distributions as function of diameter (green) and composition (blue).

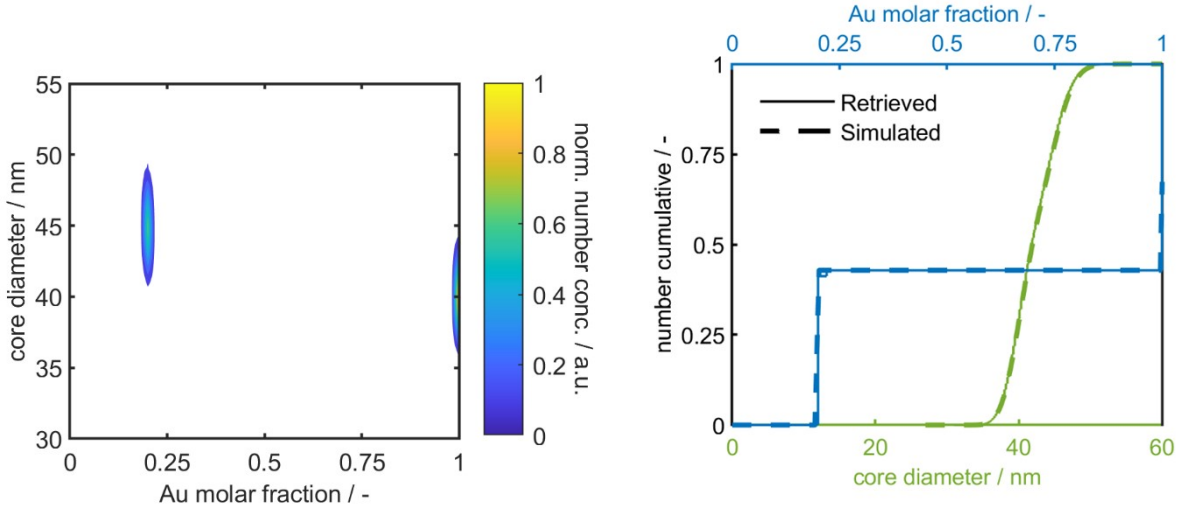

Figure S12. Left: 2D size-composition distributions for a mixture of 40 nm Au and 45 nm 20 % GMF alloy NPs obtained by OBC analysis of synthetic data. Right: Respective marginalized number weighted cumulative distributions as function of diameter (green) and composition (blue).

Reproducibility during multiwavelength (MWL) AUC experiments

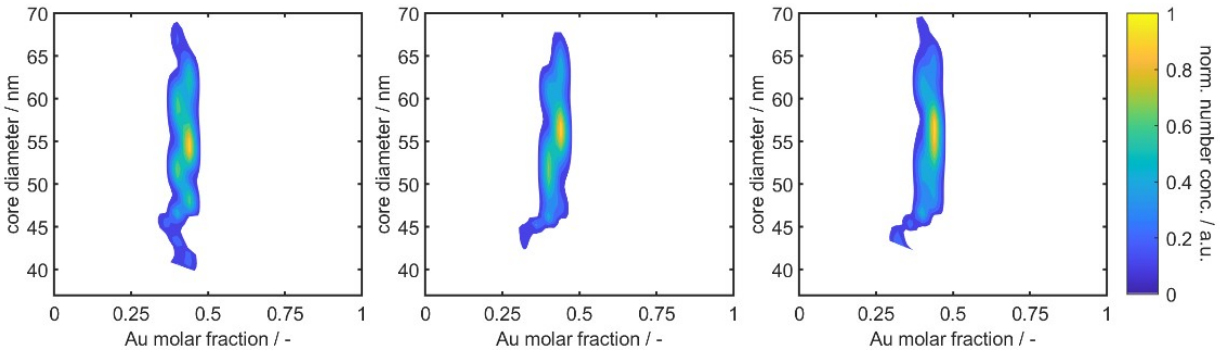

Figure S13. Size and composition distributions obtained by MWL-AUC and OBC analysis for three replicates of an alloy sample with a targeted 50 % GMF.

Shape and morphology of investigated NPs

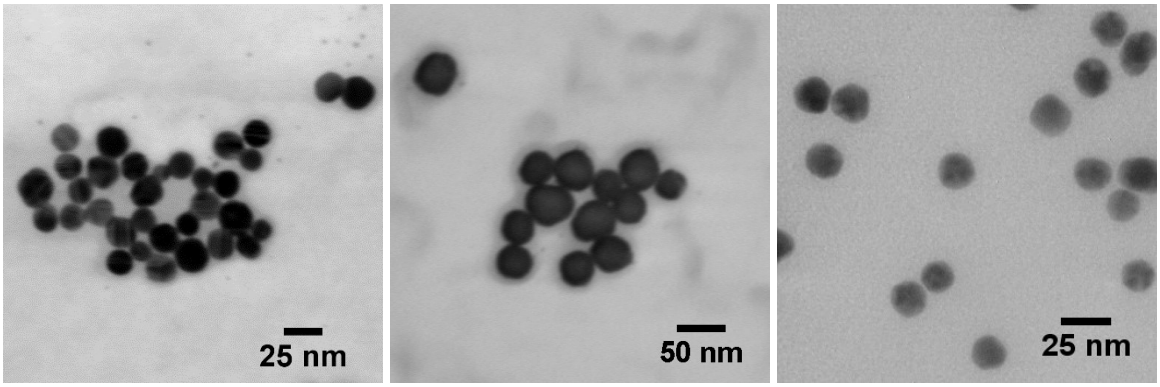

Figure S14. (S)TEM images of 20 nm Ag NPs (left), 45 nm Ag-Au 0.5 GMF alloy NPs (middle) and 20 nm Au NPs (right).

2D distributions from experimental AUC data

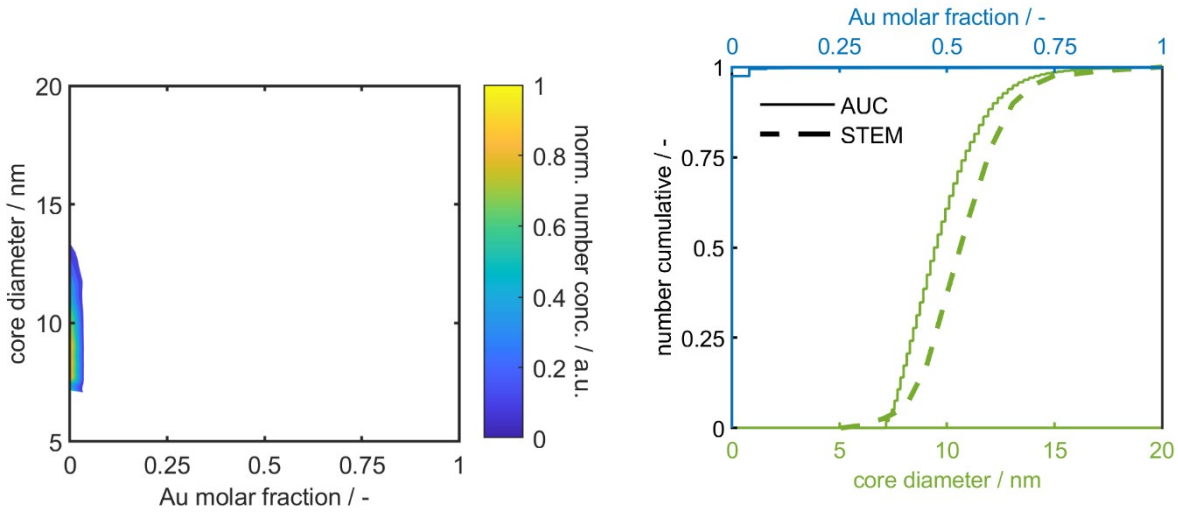

Figure S15. Left: 2D size-composition distributions for 10 nm Ag NPs obtained by OBC analysis of MWL-AUC data. Right: Respective marginalized number weighted cumulative distributions as function of diameter (green) and composition (blue).

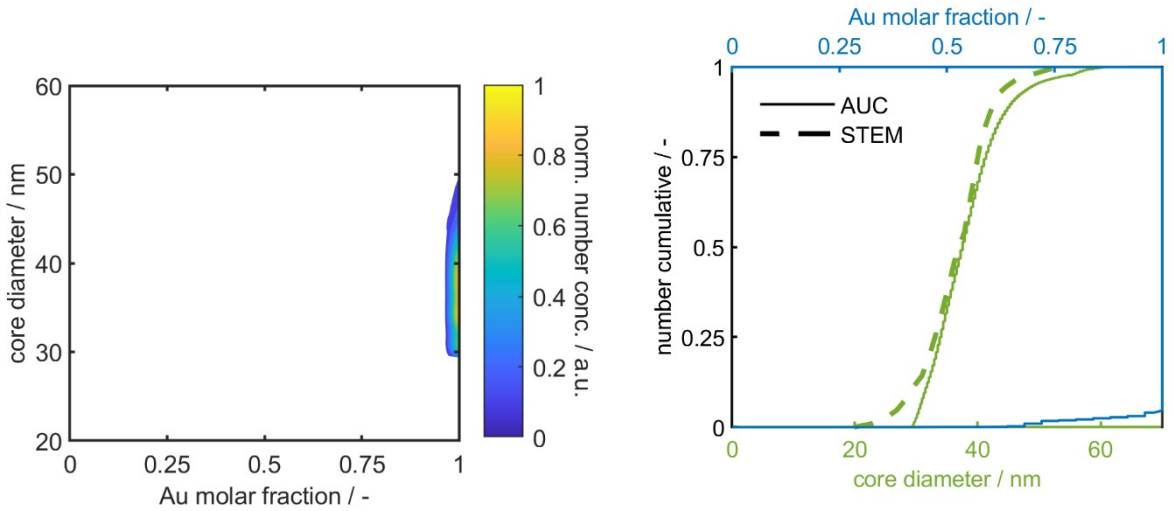

Figure S16. Left: 2D size-composition distributions for 40 nm Au NPs obtained by OBC analysis of MWL-AUC data. Right: Respective marginalized number weighted cumulative distributions as function of diameter (green) and composition (blue).

Extinction cumulative intervals selection for OBC analysis

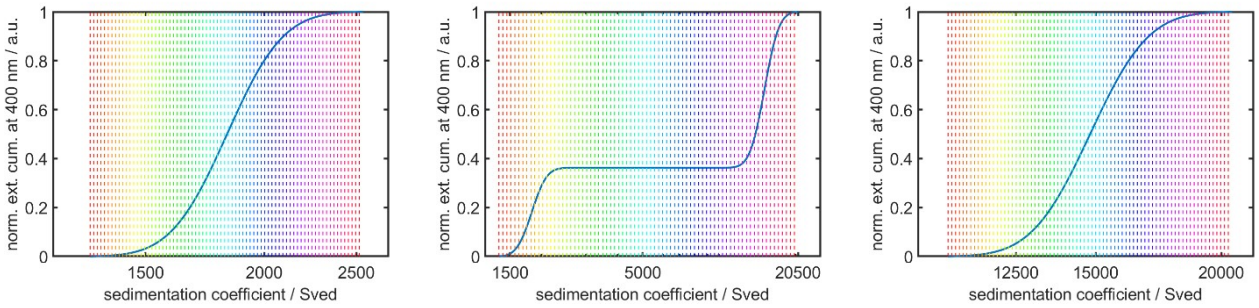

Figure S17. Extinction cumulative distribution at 400 nm and selected intervals for analysis of 20 nm Ag NPs (left), 20 nm Ag and 40 nm Au NPs (middle) and 40 nm Au and 45 nm 50 % GMF alloy NPs (right) obtained by AUC simulation.

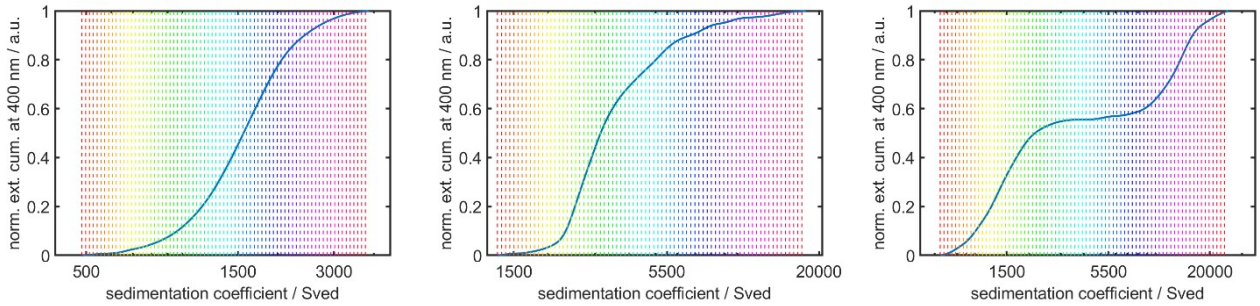

Figure S18. Extinction cumulative distribution at 400 nm and selected intervals for analysis of 20 nm Ag NPs (left), 20 nm Au NPs (middle) and mix of 20 nm Ag and 40 nm Au NPs (right) obtained by AUC experiment.

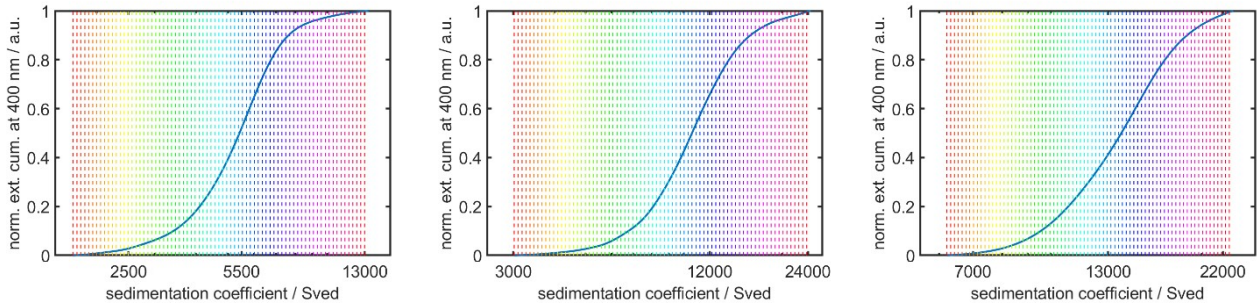

Figure S19. Extinction cumulative distribution at 400 nm and selected intervals for analysis of 30 nm 25 % GMF alloy NPs (left), 35 nm 50 % GMF alloy NPs (middle) and 40 nm Au and 42 nm 50 % GMF alloy NPs (right) obtained by AUC experiment.

References

1 U. Kreibig and M. Vollmer, *Optical Properties of Metal Clusters*, Springer, Berlin, Heidelberg, 1995.
2 U. Kreibig, *J. Phys. F: Met. Phys.*, 1974, **4**, 999–1014.
3 A. Kawabata and R. Kubo, *J. Phys. Soc. Jpn.*, 1966, **21**, 1765–1772.
4 L. Genzel, T. P. Martin and U. Kreibig, *Z Physik B*, 1975, **21**, 339–346.
5 R. Ruppin and H. Yatom, *Phys. Stat. Sol. (b)*, 1976, **74**, 647–654.
6 D. M. Wood and N. W. Ashcroft, *Phys. Rev. B*, 1982, **25**, 6255–6274.
7 W. A. Kraus and G. C. Schatz, *J. Chem. Phys.*, 1983, **79**, 6130–6139.
8 P. Apell and D. R. Penn, *Phys. Rev. Lett.*, 1983, **50**, 1316–1319.
9 P. B. Johnson and R. W. Christy, *Phys. Rev. B*, 1972, **6**, 4370–4379.
10 D. Rioux, S. Vallières, S. Besner, P. Muñoz, E. Mazur and M. Meunier, *Adv. Opt. Mater.*, 2014, **2**, 176–182.
11 K. M. McPeak, S. V. Jayanti, S. J. P. Kress, S. Meyer, S. Iotti, A. Rossinelli and D. J. Norris, *ACS Photonics*, 2015, **2**, 326–333.
12 R. P. Carney, J. Y. Kim, H. Qian, R. Jin, H. Mehenni, F. Stellacci and O. M. Bakr, *Nat. Commun.*, 2011, **2**, 335.
13 M. J. Uttinger, S. Boldt, S. E. Wawra, T. D. Freiwald, C. Damm, J. Walter, D. Lerche and W. Peukert, *Part. Part. Syst. Charact.*, 2020, **37**, 2000108.
14 T. Furia and Chemical Rubber Company., *CRC Handbook of Food Additives*, CRC Press, Cleveland, 1972.
15 M. Daimon and A. Masumura, *Appl. Optics*, 2007, **46**, 3811–3820.
16 M. A. Yurkin and A. G. Hoekstra, *J. Quant. Spectrosc. Ra.*, 2011, **112**, 2234–2247.
17 I. L. Rasskazov, P. S. Carney and A. Moroz, *OSA Contin.*, 2020, **3**, 2290.
18 Z. Y. Li, J. P. Wilcoxon, F. Yin, Y. Chen, R. E. Palmer and R. L. Johnston, *Faraday discussions*, 2008, **138**, 363-73; discussion 421-34.